Science Advances
AAAS

Supplementary Materials for

The multifunctional use of an aqueous battery for a high capacity jellyfish robot

Xu Liu *et al.*

Corresponding author: Lynden A. Archer, laa25@cornell.edu; Robert F. Shepherd, rfs247@cornell.edu

Sci. Adv. **10**, eadq7430 (2024)
DOI: 10.1126/sciadv.adq7430

The PDF file includes:

Other Supplementary Material for this manuscript includes the following:

Supplementary Text

Text S1. Characterization of materials and battery

Powder X-ray diffraction was performed on Bruker D8 Advance ECO powder diffractometer with a Cu Kα X-ray source. Field-emission scanning electron microscopy (FESEM) was carried out on Zeiss Gemini 500 Scanning Electron Microscope equipped with Bruker energy dispersive spectroscopy (EDS) detector to study the electrodeposition morphology of Zn.

We tested the stability of the Dragon Skin 30 by immersing a piece of bell (2 cm × 4 cm) in the 4 M ZnI_2 solution. By stressing it after being immersed in the solution for one day, it was still stretchable as the original piece (**Fig. S9**).

We used a Neware CT-3008 as our battery testing system. The battery cells were galvanostatically charged and discharged.

Text S2. Simulation of Jellyfish's motion and power dynamics

The fluid within the Jellyfish body is contained within the central and bell chambers, denoted as p_{in} and p_{out}, respectively. The central chamber is modelled as a piston with an effective area a_{in}. The motor inside this chamber drives a central rod of length $l_{d,r}$ cyclically, changing its effective length as follows,

$$l_{d,r}(t) = l_0 + l_{m,a}\sin(\omega t),$$

where $l_{m,a}$ is the motor arm and ω is the angular velocity of the motor. The rod is connected to the Jellyfish's outer perimeter via side rods (**see Fig. S2**), changing their angle in tandem with changes

in its effective length. This process induces a flapping motion, subsequently propelling the robot's body.

The power supplied by the motor is used to derive the viscous electrolyte through the flow battery cell, as well as propel the robot's body against forces applied by the external fluid. Therefore, the required power can be described as follows,

$$P_m(t) = a_{in}\big(p_{out}(t) - p_{in}(t)\big)v_{FB}(t) + \big(F_t(t) - F_d(t)\big)\frac{\partial x}{\partial t},$$

where P_m is the power used by the motor, v_{FB} is the mean flow through the flow battery channel, F_t is the overall propelling force exerted by the outer perimeter, F_d is the drag force acting on the top of the Jellyfish, and $x(t)$ is the robot's center of mass location.

The drag opposing the robot's motion is,

$$F_d(t) = \frac{1}{2}\pi\rho C_D\, r_{out}^2\, \dot{l}_{d,r}^2\, \mathrm{sgn}\big(\dot{l}_{d,r}\big),$$

where ρ is the surrounding fluid's density, $C_D = \rho \dot{x} r_{out}\,/\mu_o$ is the drag coefficient for a hemisphere geometry, $C_D \approx 0.42$ (36), r_{out} is the outer radius of the robot, and μ_o is the viscosity of the external fluid.

Assuming a negligible density difference between the electrolyte inside the sealed body of the robot and the surrounding fluid, the system is considered close to neutrally buoyant in the fluid, with negligible gravity effects in play. Therefore, the thrust force propelling the robot's body is counterbalanced by the drag force acting on the outer perimeter. Scaling of the thrust force as the drag on the robot during motion, where the thrust forward is stronger than the backstroke, yields,

$$F_t(t) = \frac{1}{2}\rho A_w c_d \dot{l}_{d,r}^2\, \mathrm{sgn}\big(\dot{l}_{d,r}\big)\big(\varepsilon \cdot \mathrm{sgn}\big(\dot{l}_{d,r}\big) + 1\big),$$

where A_w is the overall area of the outer perimeter, and ε stands for the asymmetry in propulsion. We assume in the model that the relation between the elastic deformation of the outer bell and the pressure can be approximated by,

$$p_{out}(t) = c_e\big(V_{out}(t) - V_{out,0}\big) + p_{ext},$$

where c_e is the elastic coefficient of the outer hemisphere, p_{ext} is the external pressure outside the robot's body, i.e., atmospheric pressure, and $V_{out,0}$ and $V_{out}(t)$ are the bell chamber's volume initially and over time, respectively. Based on the simulation, the position of the Jellyfish mass center matches well with the experimental data.

The required current for the motor's work, $I(t)$, per a constant voltage difference, ΔV_{FB}, is dictated by the power requirements as

$$I(t) = \frac{|P_m|}{\Delta V_{FB}}.$$

The viscous resistance to the flow passing through the porous electrode (**Fig. 1c**), can be described by Darcy's law (37),

$$v_{FB} = \frac{k\big(p_{out}(t) - p_{in}(t)\big)}{\mu_i\, L},$$

where k is the permeability of the material, μ_i is the dynamic viscosity of the electrolyte fluid, and L is the flow battery channel length. The relation between the average flux v_{FB} and the total fluidic volume entering (or exiting) the central chamber is $\dot{V}_{in} = h\, w\, v_{FB}$, where h and w are the height and width of the flow battery channel.

The maximal current that can be produced by the battery is denoted as the limiting current I_{lim}. We can relate the average electrolyte flux through the battery to the limiting current via (38),

$$I_{lim}(t) = c_{FB}\, n_e\, \mathrm{Cap}(t)|v_{FB}|^{0.4},$$

where $c_{FB} = 1.6 \cdot 10^{-4}\ m\ s^{-1}$ is the local mass transfer coefficient (38-40), n_e are the number of electrons involved in the redox reaction, in this case $3I^- - 2e^- \leftrightarrow I_3^-$ and the capacity of the battery is denoted $\mathrm{Cap}(t)$, is assumed to be linearly proportional to the electrolyte concentration, $C(t)$,

$$\mathrm{Cap}(t) = \frac{\mathrm{Cap}_0}{C_0} C(t),$$

where Cap_0 and C_0 are the initial values of the capacity and concentration stored in the robot's electrolyte. The electric capacity is depleted by the power consumption during the robot's operation,

$$\frac{\partial \mathrm{Cap}(t)}{\partial t} = -I(t)\Delta V_{FB}$$

The maximal power that can be provided by the flow battery to the robot is given by,

$$|P_{max}(t)| = I_{\mathrm{lim}}(t)\Delta V_{FB}$$

As long as the motor provides sufficient power, i.e. $|P_{max}(t)| > |P_{motor}(t)|$, the propulsion persists. However, once the supplied power becomes insufficient compared to the required power, the robot ceases its motion, before utilizing all the energy stored in the battery reservoir. This balance thus determines the maximal range and time of operation of the Jellyfish, see **Fig. 6b**.

Text S3. Jellyfish power and energy calculations

For the calculation of theoretical swimming time, we use the 11 Ah L^{-1} as the capacity provided the primary battery. The totally energy available for the Jellyfish's operation is 11 Ah L^{-1} * 0.4 L *

1 V * 10 cells = 44 Wh. The energy consumption comes from three sources: the motor (Pololu 4797, 85 RPM, 3.6 W), the teensy 3.2 microcontroller (DEV 13736, SparkFun Electronics, 0.15 W), and the motor driver carrier (DRV 8838, Pololu, 0.7 W). To swimming from the bottom to the top of the tank, the Jellyfish needs (3.6 W + 0.15 W + 0.7 W) * 6 s = 26.7 J. The theoretical swimming time is calculated to be 44 Wh/ (3.6 W + 0.15 W + 0.7 W) = 9.8 h. The real swimming itme of 90 min means we only use 15% of the capacity of the battery. The flow battery makes the robot achieve a SED of 44 Wh/5.3 kg = 8.3 Wh kg^{-1}. So the density of the robot is 5.3 kg/(0.8 * V_{bell} + $V_{control\ chamber}$) = 0.91 g cm^{-3}.

Text S4. Jellyfish cost calculation

The cost of the robot system mainly comes from the chemicals of the battery and 3D printed battery and robot sealings. To make the jellyfish robot, we need ZnI_2 of 4 L * 4 M = 16 mol, which costs $3,554, and Nafion cost is $100, the KI 4 L * 1 M = 4 mol ($268), and I_2 would be 4 L * 0.3 M = 1.2 mol ($291). The 3D printed robot sealings need a volume of printing resin of 362 mL and consume \$250 L^{-1} * 0.362 L = $90. The total cost of one Jellyfish is 3554 + 100 + 268 + 291 + 90 = $4,303.

Text S5. Jellyfish energy efficiency

The motor's energy is consumed both for performing work on the robot's external environment via hydrodynamic forces, as well as for overcoming the robot's internal resistance to actuation. Our calculations, taking into account this robot's characteristic values, show that the primary source of energy consumption is the cyclic forcing of large volumes of viscous liquids within the flow

battery's permeable layers, which is necessary for generating mechanical movement as well as battery operation. According to our calculations, overcoming viscous resistance accounts for approximately 95% to 98% of the total power output from the motors, resulting in very low overall efficiency for this configuration (from 2% to 4%, depending on the speed of the robot). Efficiency was calculated here as the ratio of $F_t \dot{x}_{cm}/p_m$, where F_t is the generated thrust, $\dot{x}_{cm}$ is the speed of the center of mass of the robot, and p_m is the total power by the motor. Future designs could improve this low efficiency by enabling parallel fluid flow outside of the flow-battery cell channels, or alternatively by reducing the viscous resistance within the channels.

Text S6. Potential ways to improve battery lifetime

There are two main approaches we think would help extend battery life: mechanical and electrochemical pathways.

Mechanical approach: This involves increasing the energy storage by increasing the electrolyte concentration and volume to provide more reaction species, or enhancing the area of the electrode to allow more space for Zn deposition. In our battery, the highest area capacity of 110 mAh cm^{-2} mainly limits the operation time. Therefore, we can improve the battery's lifetime by increasing the electrode area to accommodate more Zn deposition. This can be achieved by either increasing the size of the battery or connecting more batteries in parallel. Our battery is 0.55 cm each in thickness, making this approach relatively straightforward to implement.

Electrochemical approach: This involves optimizing the battery design to minimize ohmic resistance, maximize electrolyte transport, and enhance the surface area and activity of the electrodes. Such improvements can lead to a significant increase in the energy density of the battery, thereby extending its lifetime.

Supplementary Figures

Fig. S1. The assembled Jellyfish powered by $ZnBr_2$ flow battery illuminated in darkness.

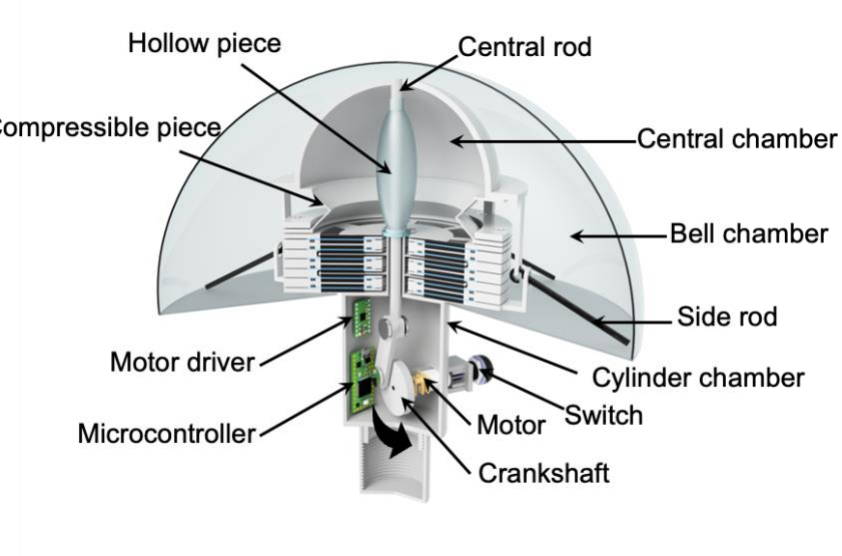

Fig. S2.The Jellyfish actuation system design.

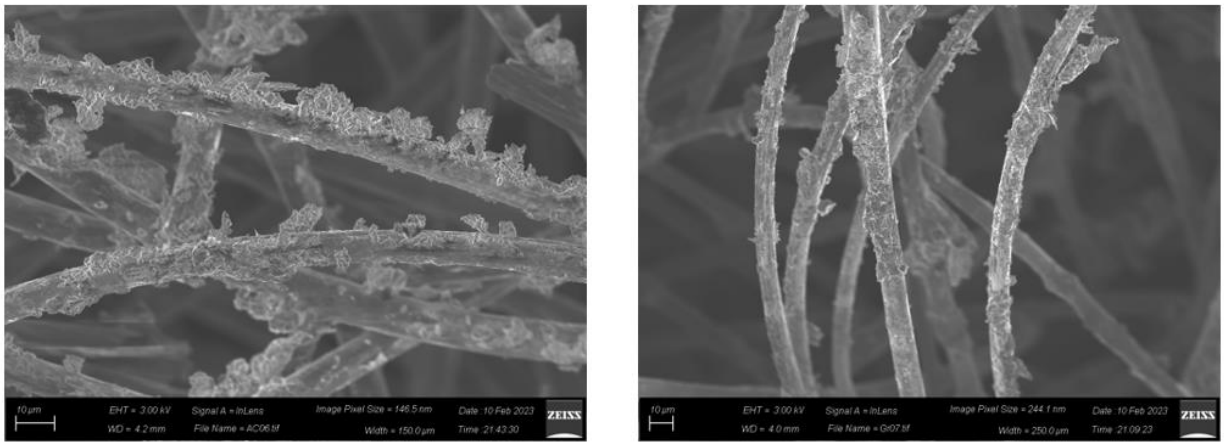

Fig. S3. SEM images of carbon felt after active carbon treatment.

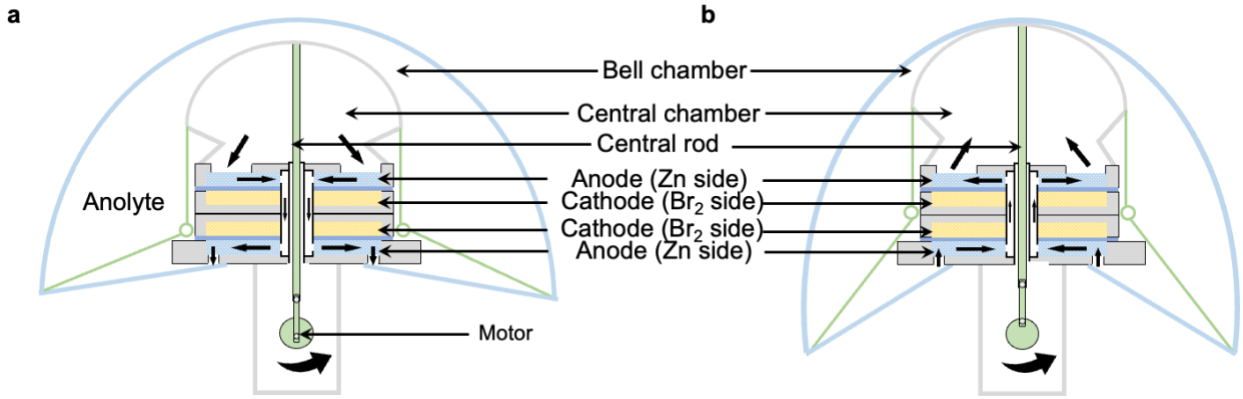

Fig. S4. The battery operation process of the Jellyfish. a, The motor pulls down the central rod and compresses the central chamber to push electrolyte flow from central chamber to bell chamber. **b,** The motor pushes up the central rod and decompresses the central chamber to push electrolyte flow from bell chamber to central chamber.

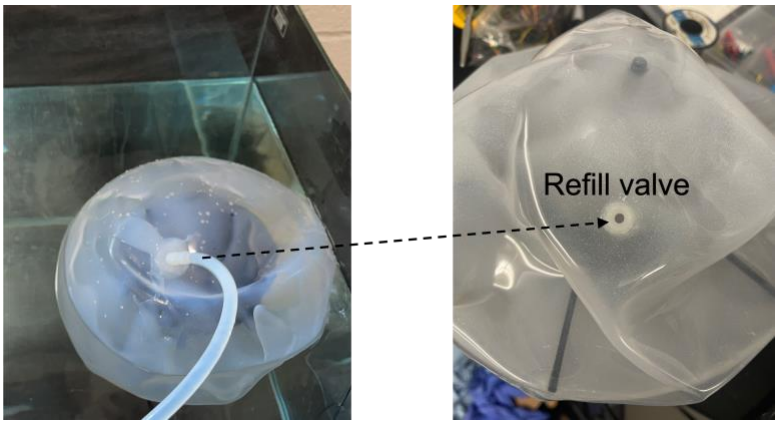

Fig. S5. The refill valve used for rapid recharging of primary rechargeable ZnI_2 battery.

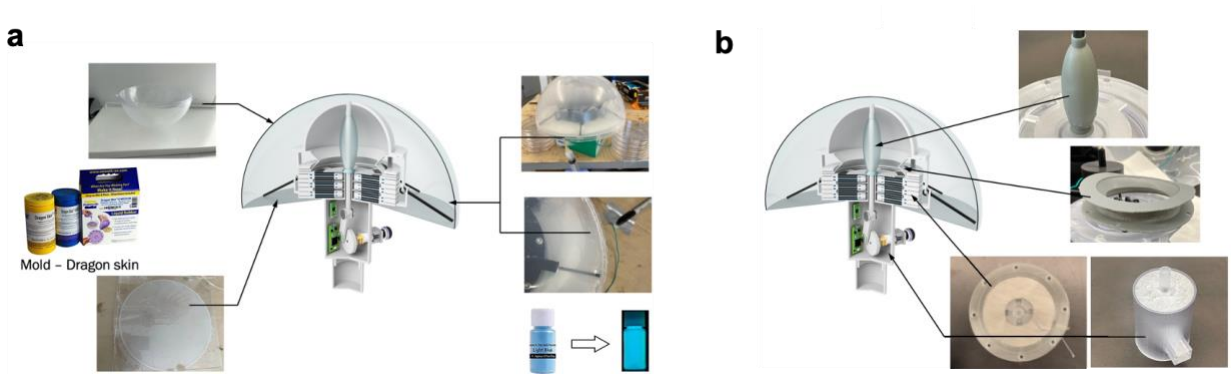

Fig. S6. The manufacturing process of the Jellyfish. a, Bell manufacturing. **b,** SIL and current collector (Ti mesh) bonding.

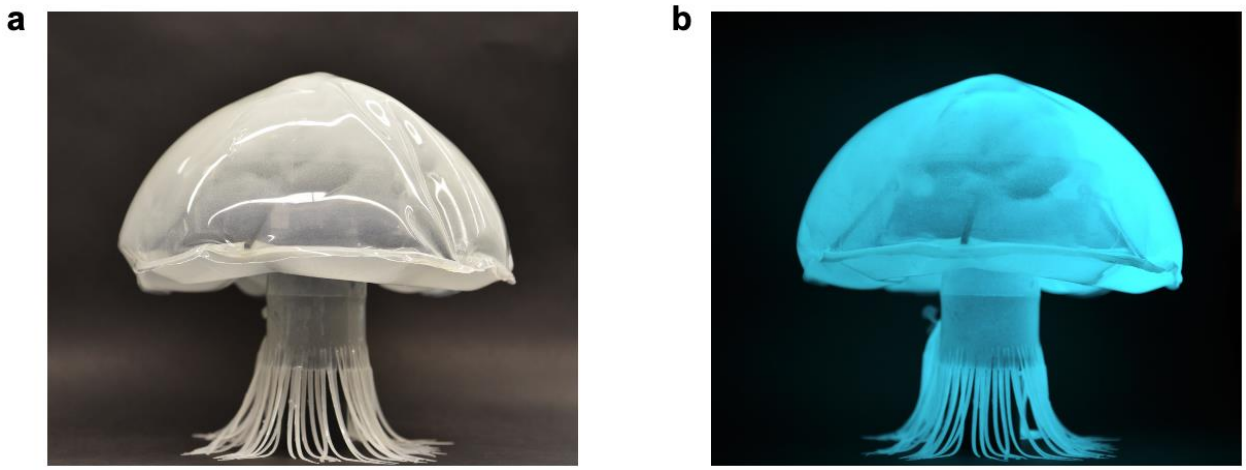

Fig. S7. The Jellyfish without electrolyte under different illumination conditions. a, daylight conditions, and **b,** darkness conditions.

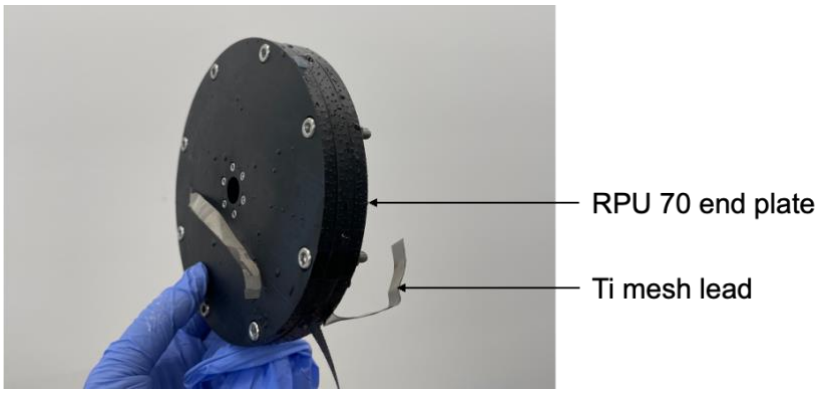

Fig. S8. The single battery cell with labelled components.

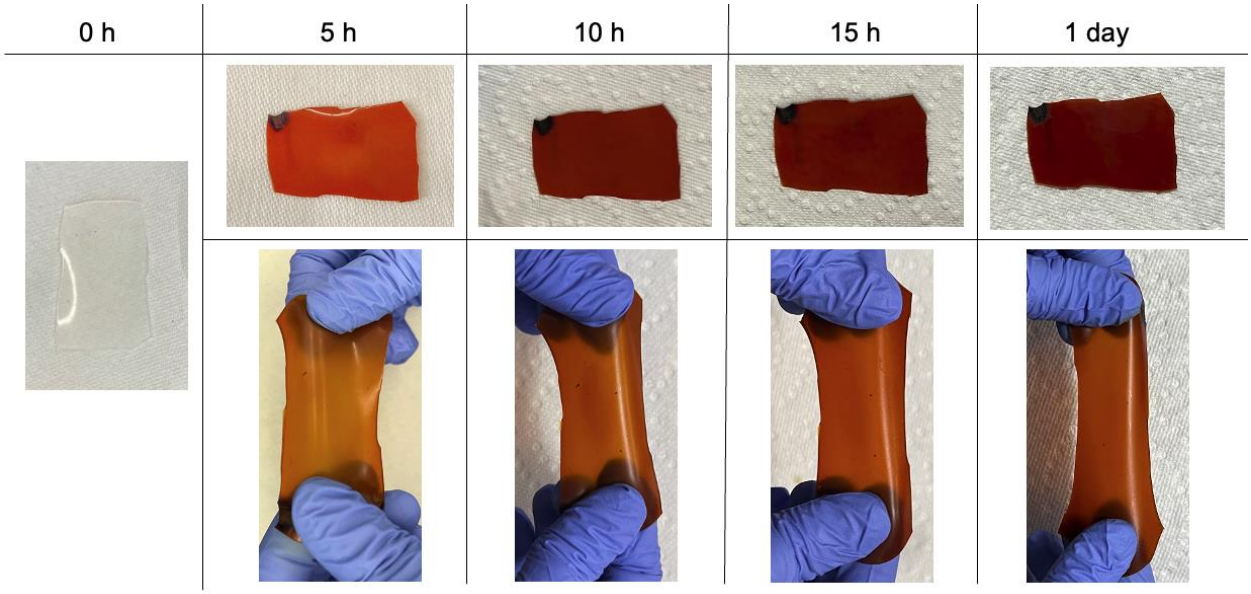

Fig. S9. The bell material test after being immersed in the reacted electrolyte for 5 h, 10 h, 15 h, 1 day.

Supplementary Table

Table S1: The simulation parameter settings.

Parameter	Notation	Value [units]
Initial driving rod length	l_0	0.2 [m]
Motor arm length	$l_{m,a}$	0.01 [m]
The inner radius of the robot	r_{in}	0.04 [m]
The outer radius of the robot	r_{out}	0.1 [m]
External fluid's density	ρ	10^3 [kg/m^3]
External fluid's viscosity	μ	$8.9 \cdot 10^{-4}$ [kg/m^3]
Central chamber initial volume	$v_{in,0}$	$4 \cdot 10^{-3}$ [m^3]
Motor angular velocity	ω	5.28 [rad/s]
Drag coefficient – hemisphere	C_D	0.43
Propulsion asymmetry	ε	0.4
Battery voltage	ΔV_{FB}	1.6 [V]
Battery cell height	h	0.01 [m]
Battery cell width	w	0.025 [m]
Battery cell length	L_{FB}	0.05 [m]
Porous electrode permeability	k	$6.3 \cdot 10^{-8}$ [m^2]
Initial battery capacity	Cap_0	48,960 [A · s]
Initial electrolyte concentration	C_0	4 [mole]
Number of electrons involved in the redox reaction	n_e	2

Supplementary Videos

- Supplementary Video 1: The jellyfish robot swimming powered by $ZnBr_2$ flow battery
- Supplementary Video 2: The jellyfish robot dark environment swimming powered by $ZnBr_2$ flow battery
- Supplementary Video 3: The jellyfish robot swimming powered by ZnI_2 flow battery

Supplementary Data

- Supplementary Simulation Data (Jellyfish swimming simulation)

REFERENCES AND NOTES

1. G. Z. Yang, J. Bellingham, P. E. Dupont, P. Fischer, L. Floridi, R. Full, N. Jacobstein, V. Kumar, M. McNutt, R. Merrifield, B. J. Nelson, B. Scassellati, M. Taddeo, R. Taylor, M. Veloso, Z. L. Wang, R. Wood, The grand challenges of science robotics. *Sci. Robot.* **3**, eaar7650 (2018).

2. N. T. Jafferis, E. F. Helbling, M. Karpelson, R. J. Wood, Untethered flight of an insect-sized flapping-wing microscale aerial vehicle. *Nature* **570**, 491–495 (2019).

3. Z. L. Wang, Triboelectric nanogenerators as new energy technology for self-powered systems and as active mechanical and chemical sensors. *ACS Nano* **7**, 9533–9557 (2013).

4. M. Wang, D. Vecchio, C. Wang, A. Emre, X. Xiao, Z. Jiang, P. Bogdan, Y. Huang, N. A. Kotov, Biomorphic structural batteries for robotics. *Sci. Robot.* **5**, eaba1912 (2020).

5. M. T. Tolley, R. F. Shepherd, B. Mosadegh, K. C. Galloway, M. Wehner, M. Karpelson, R. J. Wood, G. M. Whitesides, A resilient, untethered soft robot. *Soft Robot.* **1**, 213–223 (2014).

6. X. Huang, K. Kumar, M. K. Jawed, A. Mohammadi Nasab, Z. Ye, W. Shan, C. Majidi, Highly dynamic shape memory alloy actuator for fast moving soft robots. *Adv. Mater. Technol.* **4**, 1800540 (2019).

7. A. D. B. L. Ferreira, P. R. O. Nóvoa, A. T. Marques, Multifunctional material systems: A state-of-the-art review. *Compos. Struct.* **151**, 3–35 (2016).

8. N. Kottege, C. Parkinson, P. Moghadam, A. Elfes, S. P. N. Singh, in *2015 IEEE International Conference on Robotics and Automation (ICRA)* (IEEE, 2015), pp. 5140–5147.

9. Z. Zhakypov, K. Mori, K. Hosoda, J. Paik, Designing minimal and scalable insect-inspired multi-locomotion millirobots. *Nature* **571**, 381–386 (2019).

10. T. Li, G. Li, Y. Liang, T. Cheng, J. Dai, X. Yang, B. Liu, Z. Zeng, Z. Huang, Y. Luo, T. Xie, W. Yang, Fast-moving soft electronic fish. *Sci. Adv.* **3**, e1602045 (2017).

11. A. J. Ijspeert, A. Crespi, D. Ryczko, J.-M. Cabelguen, From swimming to walking with a salamander robot driven by a spinal cord model. *Science* **315**, 1416–1420 (2007).

12. H. Kim, J. Choi, K. K. Kim, P. Won, S. Hong, S. H. Ko, Biomimetic chameleon soft robot with artificial crypsis and disruptive coloration skin. *Nat. Commun.* **12**, 4658 (2021).

13. G. Li, X. Chen, F. Zhou, Y. Liang, Y. Xiao, X. Cao, Z. Zhang, M. Zhang, B. Wu, S. Yin, Y. Xu, H. Fan, Z. Chen, W. Song, W. Yang, B. Pan, J. Hou, W. Zou, S. He, X. Yang, G. Mao, Z. Jia, H. Zhou, T. Li, S. Qu, Z. Xu, Z. Huang, Y. Luo, T. Xie, J. Gu, S. Zhu, W. Yang, Self-powered soft robot in the Mariana Trench. *Nature* **591**, 66–71 (2021).

14. D. Lin, Y. Liu, Y. Cui, Reviving the lithium metal anode for high-energy batteries. *Nat. Nanotechnol.* **12**, 194–206 (2017).

15. K. T. Nam, D.-W. Kim, P. J. Yoo, C.-Y. Chiang, N. Meethong, P. T. Hammond, Y.-M. Chiang, A. M. Belcher, Virus-enabled synthesis and assembly of nanowires for lithium ion battery electrodes. *Science* **312**, 885–888 (2006).

16. M. Wehner, R. L. Truby, D. J. Fitzgerald, B. Mosadegh, G. M. Whitesides, J. A. Lewis, R. J. Wood, An integrated design and fabrication strategy for entirely soft, autonomous robots. *Nature* **536**, 451–455 (2016).

17. C. A. Aubin, S. Choudhury, R. Jerch, L. A. Archer, J. H. Pikul, R. F. Shepherd, Electrolytic vascular systems for energy-dense robots. *Nature* **571**, 51–57 (2019).

18. X. Yang, L. Chang, N. O. Perez-Arancibia, An 88-milligram insect-scale autonomous crawling robot driven by a catalytic artificial muscle. *Sci. Robot.* **5**, eaba0015 (2020).

19. C. A. Aubin, R. H. Heisser, O. Peretz, J. Timko, J. Lo, E. F. Helbling, S. Sobhani, A. D. Gat, R. F. Shepherd, Powerful, soft combustion actuators for insect-scale robots. *Science* **381**, 1212–1217 (2023).

20. C. A. Aubin, B. Gorissen, E. Milana, P. R. Buskohl, N. Lazarus, G. A. Slipher, C. Keplinger, J. Bongard, F. Iida, J. A. Lewis, R. F. Shepherd, Towards enduring autonomous robots via embodied energy. *Nature* **602**, 393–402 (2022).

21. R. A. Watson, S. G. Ficici and J. B. Pollack, Embodied evolution: Distributing an evolutionary algorithm in a population of robots. *Robot. Auton. Syst.* **39**, 1–18 (2002).

22. W. M. Megill, J. M. Gosline and R. W. Blake, The modulus of elasticity of fibrillin-containing elastic fibres in the mesoglea of the hydromedusa *Polyorchis penicillatus*. *J. Exp. Biol.* **208**, 3819–3834 (2005).

23. Y. Yao, J. Lei, Y. Shi, F. Ai, Y.-C. Lu, Assessment methods and performance metrics for redox flow batteries. *Nat. Energy* **6**, 582–588 (2021).

24. D. Chao, W. Zhou, F. Xie, C. Ye, H. Li, M. Jaroniec, S.-Z. Qiao, Roadmap for advanced aqueous batteries: From design of materials to applications. *Sci. Adv.* **6**, eaba4098 (2020).

25. S. Jin, J. Yin, X. Gao, A. Sharma, P. Chen, S. Hong, Q. Zhao, J. Zheng, Y. Deng, Y. L. Joo, L. A. Archer, Production of fast-charge Zn-based aqueous batteries via interfacial adsorption of ion-oligomer complexes. *Nat. Commun.* **13**, 2283 (2022).

26. B. Li, Z. Nie, M. Vijayakumar, G. Li, J. Liu, V. Sprenkle, W. Wang, Ambipolar zinc-polyiodide electrolyte for a high-energy density aqueous redox flow battery. *Nat. Commun.* **6**, 6303 (2015).

27. R. V. Adith, R. P. Naresh, K. Mariyappan, M. Ulaganathan, P. Ragupathy, An optimistic approach on flow rate and supporting electrolyte for enhancing the performance characteristics of Zn-Br2 redox flow battery. *Electrochim. Acta* **388**, 138451 (2021).

28. Z. Pei, Z. Zhu, D. Sun, J. Cai, A. Mosallanezhad, M. Chen, G. Wang, Review of the $I^-/I3^-$ redox chemistry in Zn-iodine redox flow batteries. *Mater. Res. Bull.* **141**, 111347 (2021).

29. J. Zheng, Q. Zhao, T. Tang, J. Yin, C. D. Quilty, G. D. Renderos, X. Liu, Y. Deng, L. Wang, D. C. Bock, C. Jaye, D. Zhang, E. S. Takeuchi, K. J. Takeuchi, A. C. Marschilok, L. A. Archer, Reversible epitaxial electrodeposition of metals in battery anodes. *Science* **366**, 645–648 (2019).

30. J. Zheng, L. A. Archer, Crystallographically textured electrodes for rechargeable batteries: Symmetry, fabrication, and characterization. *Chem. Rev.* **122**, 14440–14470 (2022).

31. S. Jin, Y. Shao, X. Gao, P. Chen, J. Zheng, S. Hong, J. Yin, Y. L. Joo, L. A. Archer, Designing interphases for practical aqueous zinc flow batteries with high power density and high areal capacity. *Sci. Adv.* **8**, eabq4456 (2022).

32. P. Bai, M. Z. Bazant, Performance and degradation of a lithium-bromine rechargeable fuel cell using highly concentrated catholytes. *Electrochim. Acta* **202**, 216–223 (2016).

33. V. Viswanathan, A. H. Epstein, Y.-M. Chiang, E. Takeuchi, M. Bradley, J. Langford, M. Winter, The challenges and opportunities of battery-powered flight. *Nature* **601**, 519–525 (2022).

34. Y. Li, L. Li, Y. Zhao, C. Deng, Z. Yi, D. Xiao, N. Mubarak, M. Xu, J. Li, G. Luo, Q. Chen, J. K. Kim, Homogenizing zn deposition in hierarchical nanoporous cu for a high-current, high areal-capacity Zn flow battery. *Small* **19**, e2303005 (2023).

35. S. Subbaraya, A. Breitenmoser, A. Molchanov, J. Muller, C. Oberg, D. A. Caron, G. S. Sukhatme, Circling the seas: Design of lagrangian drifters for ocean monitoring. *IEEE Robot. Autom. Mag.* **23**, 42–53 (2016).

36. P. Wegener, *What makes airplanes fly?: History, Science, and Applications of Aerodynamics* (Springer Science & Business Media, 1997).

37. J. Bear, M. Y. Corapcioglu, eds., *Fundamentals of Transport Phenomena in Porous Media* (Springer Science & Business Media, 2012), vol. 82.

38. A. Tang, B. Jie, M. Skyllas-Kazacos. Studies on pressure losses and flow rate optimization in vanadium redox flow battery. *J. Power Sources* **248**, 154–162 (2014).

39. Schmal, D., J. Van Erkel, P. J. Van Duin. Mass transfer at carbon fibre electrodes. *J. Appl. Electrochem.* **16**, 422–430 (1986).

40. X. Ma, H. Zhang, F. Xing. A three-dimensional model for negative half cell of the vanadium redox flow battery. *Electrochim. Acta* **58**, 238–246 (2011).